AIAA JOURNAL
Vol. 48, No. 7, July 2010

Three-Dimensional Modeling of Magnetic Nozzle Processes

Heath Lorzel* and Pavlos G. Mikellides†
Arizona State University, Tempe, Arizona 85281

DOI: 10.2514/1.J050123

Simulations of plasma flow through a magnetic nozzle were conducted using the time-dependent, three-dimensional magnetohydrodynamics code MACH3. Modeling of magnetic nozzle flow using constant, classical isotropic, and classical tensor resistivity provides preliminary quantitative depiction of the core-plasma flow, evolution of the magnetic field, and conversion of stagnation enthalpy to directed exhaust thrust energy, and serves as verification for the numerical model. For stagnation conditions of 100 eV and 0.355 MPa, steady-state modeling using helium propellant demonstrates a nearly isentropic expansion through the nozzle to exhaust speeds near 160 km/s. The extent of the contribution from the magnetic diffusion and the mass-flux penetration to the thickness of the current layer strongly depends on plasma resistivity. Plasma-field interaction results in a reduction of approximately 50% of the directed axial thrust when compared with a solid-wall nozzle of equivalent Mach number design. At fixed plasma pressure and applied field the exhaust velocity scales appropriately as the square root of the stagnation temperature.

Nomenclature

A	=	cross-sectional area, m^2
B	=	magnetic field, T
B_0	=	magnetic field at coil center, T
J_B	=	magnet coil current, A
L_B	=	magnet coil length, m
M	=	Mach number
N	=	magnet coil turns/length, m^{-1}
P	=	pressure, Pa
P_{mag}	=	magnetic pressure, Pa
R	=	radius, m
R_B	=	magnet coil radius, m
R_m	=	magnetic Reynolds number
T	=	thrust, N
T_e	=	temperature, eV
U_{ex}	=	exhaust velocity, m/s
u	=	velocity vector, m/s
α	=	diffusivity, m^2/s
γ	=	ratio of specific heats
Λ	=	maximum impact parameter
δ	=	current layer thickness, m
η	=	resistivity, Ω-m
η_{eff}	=	thrust efficiency
ρ	=	density, kg/m^3
ρ_0	=	stagnation density, kg/m^3
τ	=	characteristic time, s
ω_B	=	cyclotron frequency, s^{-1}

I. Introduction

THERMONUCLEAR fusion is a primary projected energy source capable of satisfying the requirements for a propulsion system that will allow for extensive human exploration of the solar system and significantly decrease travel times for interplanetary missions. Williams and Borowski [1] demonstrate that for a 118 day trip delivering 172 metric tons of payload to a Jupiter rendezvous the requirements for a propulsion system are $U_{\text{ex}} \sim 347$ km/s and $T \sim 27.8$ kN for a nearly straight-line, continuous thrust mission. Fusion reactants can be mixed with much higher mass flows of cold propellant to produce optimized exhaust speeds. The fusion-heated propellant reaches stagnation temperatures well in excess of 100 eV. Confinement and acceleration of such high temperature propellant requires a magnetic nozzle, a properly shaped magnetic field capable of guiding the flow to high exhaust speeds while maintaining tolerable thermal loads to the surrounding walls.

The operation of the magnetic nozzle in propulsion systems requires the formation of a current layer around the plasma. This is generated by the pressure-gradient force acting across the confining applied field. Under idealized conditions, i.e., a zero thickness current layer, interaction of this current with the magnetic field is just sufficient to stop the fluid motion across the field, leading to a state of magnetohydrodynamic (MHD) equilibrium. For resistive MHD, the interaction of the plasma and the magnetic field is subject to a wide variety of convective and diffusive processes which jeopardize the preservation of the current layer. Many of the processes, which may lead to instabilities, exhibit an inherent three-dimensional nature, and thus require three-dimensional simulations to accurately resolve the current layer.

The extent to which the plasma and magnetic field intermix determines the thickness of the current layer and thus the conversion of the supplied enthalpy to thrust energy. Accurate resolution of the interface requires numerical simulations and experimental analysis to quantify the power losses. Interrogation of the 3-D plasma and magnetic field distributions provides insights as to the feasibility of the model, the prevailing physical interactions, and relevant performance of the magnetic rocket.

II. Physical Model and Upgrades to the Numerical Code

A collisional plasma can be guided through a properly shaped magnetic field to create a magnetic nozzle. A finite-length solenoid supplies the magnetic field that confines the plasma during nozzle transit. This confinement behaves as a magnetic guide that decreases the area of the flow, accelerating the plasma to $M = 1$ near the center of the solenoid before allowing the plasma to expand to supersonic speeds at the exit. The field serves to accelerate the plasma in the same fashion as a converging–diverging nozzle.

A. Magnetohydrodynamics Code MACH3

Numerical simulation of plasma flow through the magnetic nozzle was made possible by the use of the time-dependent, three-dimensional, nonideal MHD code MACH3 [2]. The code solves the dynamic, single-fluid, MHD equations in all three dimensions and is

Received 7 August 2009; 3 March 2010; 4 April 2010.

*Graduate Research Assistant, Mechanical and Aerospace Engineering Department. Student Member AIAA.
†Associate Professor, Department of Engineering. Senior Member AIAA.

an upgraded version of the two-and-one-half-dimensional code MACH2 [3].

MACH3 is an arbitrary Lagrangian–Eulerian code. The hydrodynamic algorithm allows the code to be run at rest in the laboratory frame (Eulerian), at rest in the fluid frame (Lagrangian), or independently of the fluid. Furthermore, the code is equipped with adaptive mesh routines that can adjust to regions of varying characteristic scales. Such capability is essential and was used to properly resolve regions of sharp field gradient. The plasma flow was modeled using fully doubly ionized Helium. In addition to the mass and momentum conservation equations, the energy equations for electrons and ions allowed for resistive heating while assuming thermal equilibrium between species. The evolution of the magnetic field during plasma transit was computed based on a magnetic induction equation which combines Maxwell's equation and Ohm's law. The present simulations did not include the effects of anomalous resistivity, the Hall term, or thermoelectric contributions to the electric field to produce numerical solutions that can be verified by comparisons to closed-form analytic solutions and isolate the physical significance of magnetic diffusivity relative to convective transport in the shape and evolution of current layer.

B. Setup of the Simulation

The design closely followed previous simulations [4] using two-dimensional codes that focused on the requirements of $T_0 = 100$ eV, $\rho_0 = 5\text{e}-5$ kg/m^3 (stagnation pressure $P_0 = 0.355$ MPa), and a projected exhaust velocity $U_{ex} = 170$ km/s. Isentropic expansion of doubly ionized helium implies a projected exhaust temperature $T_e = 20.12$ eV, Mach number $M_e = 3.45$, and radius ratio (exhaust-to-throat) of the converging–diverging magnetic nozzle $R_e/R_* = 2$. Anticipation of future experiments using a specific vacuum tank constrains the size of the simulated computational region to a 1 m long cylindrical tube with a radius of 0.18 m. The solenoidal magnetic coil radius was chosen as $R_B = 20$ cm and the length $L_B = 32$ cm. For a finite length solenoid the field at the centerline halfway down the length of the solenoid can be approximated by

$$B_0 = \frac{L_B}{\sqrt{L_B^2 + 4R_B^2}}\mu_0 N J_B \tag{1}$$

The interaction of the plasma with the magnetic field involves numerous physical processes, and thus the characteristics of the flow as it relates to a converging–diverging nozzle, such as throat area, are impossible to determine before running the simulation. Varying the strength of the magnetic field will, in turn, vary the nozzle parameters. As a first-order approximation, the vacuum magnetic pressure at the centerline was equated to the stagnation pressure $B_B^2/2\mu_0 = P_0$, which yields a magnetic field of $0.944T$. Using $N = 100$ turns/length and Eq. (1) gives the magnetic coil current $J_B = 12.04$ kA (Fig. 1).

The computational region consisted of a $32 \times 36 \times 130$ (radial × azimuthal × axial) partitioned into 30 block-like subdomains, which are mapped to logical rectangular blocks that constitute the computational region (6 blocks in the azimuthal direction each representing 60 deg times 5 blocks in the axial direction). The computational region also included a small inner boundary at the centerline of the nozzle of radius 1.0 cm to avoid the singularity that results from a cylindrical structural mesh. This region consists of approximately 0.3% of the total cross-sectional area of the nozzle and occurs in a region where strong plasma and magnetic field gradients do not exist, and thus it does not affect the results of the simulations. Figure 2 depicts the plasma pressure profiles for a previous 2-D simulation and a current 3-D simulation, showing that the uniformity of the flow near $r = 0$ is not affected by the centerline hole, and thus this approximation does not affect the overall results of the simulations.

The outer boundary was set to zero gradients for the temperature and density with the velocity set to purely axial flow at the centerline and a no slip condition on the outer boundary (to allow diffusion of the magnetic field into the flow). The temperature and density at the inlet boundary were set to stagnation conditions with no constraint on the velocity (essentially a pressure/temperature reservoir). All values at the exit boundary were set to zero gradient with no constraint on the velocity, and thus the plasma was allowed to expand freely out the exit.

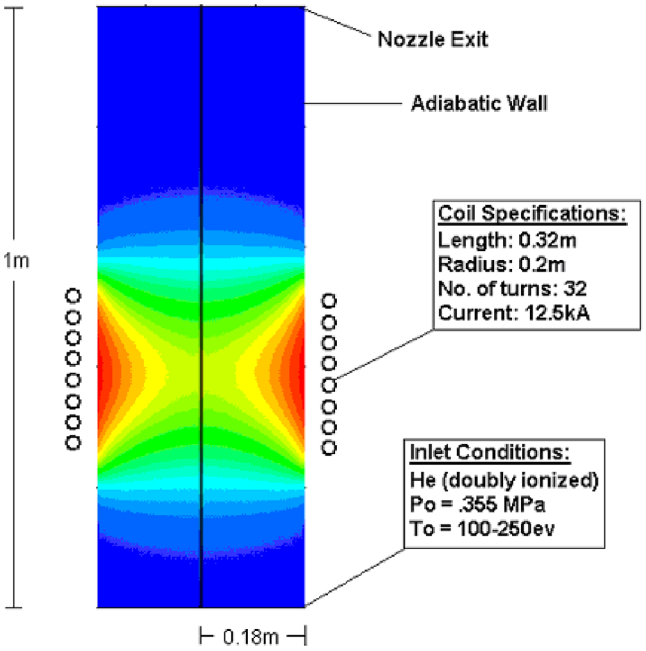

Fig. 1 Magnetic nozzle geometry and specifications. The contour plot shows the initial vacuum magnetic pressure distribution. The value at the centerline and halfway through the solenoid is $P_{mag} = 0.355$ MPa.

The plasma was modeled as an ideal gas with $\gamma = 5/3$, which is sufficient since the flow is fully doubly ionized helium. The model used the adaptive grid capabilities in the r-z plane of the code to concentrate grid points within the current layer, which is the main feature of interest in these simulations. Early simulations identified the need to resolve this feature to improve accuracy. The gradient exists in the radial and axial directions only, and thus the adaptive grid does not conform to any gradients in the azimuthal direction, which would be a result of numerical effects.

1. *Initial Magnetic Field and Boundary Conditions*

The magnetic field is supplied by an external coil (Fig. 1). The algorithm used to compute the solenoidal magnetic field was adapted from a numerical two-dimensional version which incorporates the Biot-Savart law integrating individual current-carrying coil contributions and using a vector sum over the number of turns. The axial and radial magnetic field in each individual computational cell is computed using

$$B_r(r,z) = \frac{\mu_0 I}{2\pi}\left[\frac{z}{r\sqrt{(a+r)^2+z^2}}\right]\left[-K(c) + \frac{a^2+r^2+z^2}{(a-r)^2+z^2}E(c)\right] \tag{2}$$

and

$$B_z(r,z) = \frac{\mu_0 I}{2\pi}\left[\frac{1}{\sqrt{(a+r)^2+z^2}}\right]\left[\frac{a^2-r^2-z^2}{(a-r)^2+z^2}E(c) + K(c)\right] \tag{3}$$

where $K(c)$ and $E(c)$ are elliptical integrals of the first and second kind, respectively [5]. The magnetic diffusion subroutines use ghost cells around the outer boundary of the nozzle to supply the magnetic field throughout the simulation.

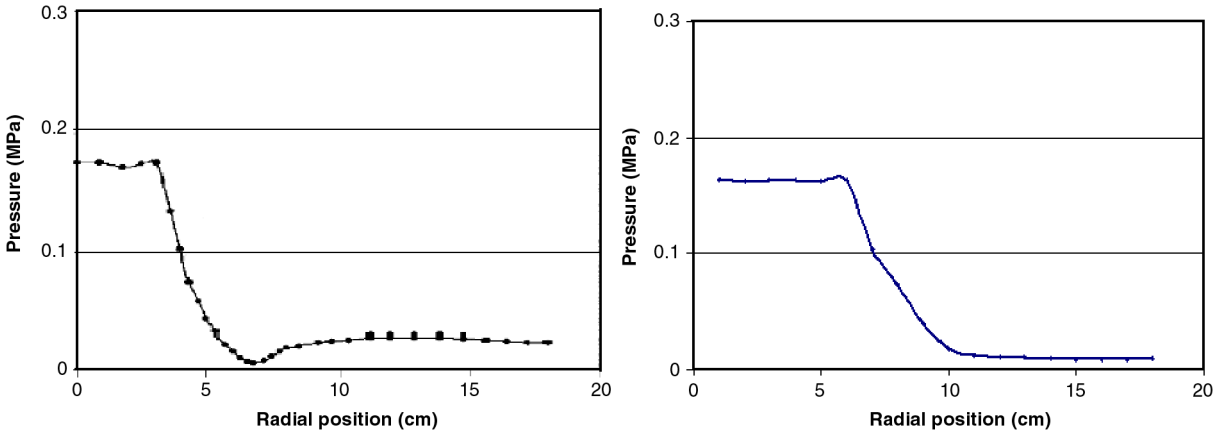

Fig. 2 Depiction of the plasma pressure profiles as a function of radial position for a previous 2-D simulation (left) and a current 3-D simulation. A comparison of the two plots illustrates the small centerline hole does not alter the uniformity of the flow near $r = 0$.

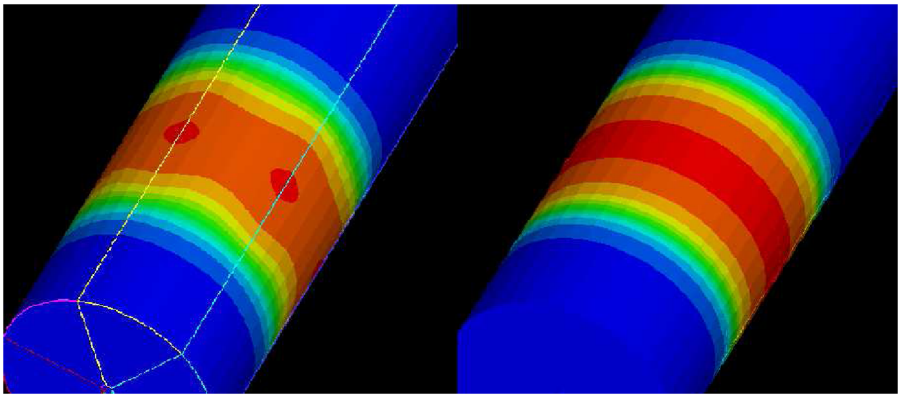

Fig. 3 A depiction of the initial magnetic field near the outer boundary of the computational region. The axisymmetry, which is artificially distorted by the nonuniform ghost cells created by MACH3 (left), is recovered by the advanced GridGen3D grid generator (right).

2. *Generation of the Computational Mesh*

The three-dimensional computational grid used in MACH3 uses a series of logical blocks that partition the physical region into subdomains, defined by specifying the location and shape of the edges, and the computational mesh which is generated within the interior of each block. For the current work, the initial computational mesh was generated using GridGen3D [6] and imported into the MACH3 code. The utilization of GridGen3D instead of the internal mesh generation subroutines in MACH3 proved essential to ensure axisymmetry of the initial grid, which in turn ensured the axisymmetry of the initial magnetic field. Specifically, the MACH3 grid generator created ghost cells of varying size and shape surrounding the outer boundary of the computational region. Since these ghost cells are responsible for allowing the magnetic field from the solenoid to diffuse into computational region, the variations destroyed the axisymmetry of the magnetic induction at the outer edge (Fig. 3). The fine control of the grid in GridGen3D allowed for the creation of uniform ghost cells, solving this problem.

3. *Adaptive Mesh*

The adaptive mesh subroutines within MACH3 use an elliptic-partial-differential-equation scheme to generate a new computational mesh each cycle based on input parameters for orthogonality, volume control, and smoothness. In addition, the adaptive mesh contains options for concentrating the grid in areas of high gradients of physical functions to capture fine-scale processes within a region of interest. The adaptive grid capabilities of MACH3 are essential for simulations of magnetic nozzle processes to accurately model the steep magnetic field gradients within the current layer.

Because the mesh will be used to capture physical gradients in the radial and axial directions only, the adaptive grid subroutine from MACH2 was modified and inserted into MACH3 to be used for this simulation. Essentially, each slice of the grid along lines of constant theta was treated as a two-dimensional MACH2 mesh, with r and z coordinates treated as x and y coordinates. The grid points are then allowed to dynamically adapt to the time-dependent physical functions in the r and z directions to accurately depict the current layer (Fig. 4). The complete system of equations is described in Brackbill [7] and its implementation for the 2-D subroutine used here is in Frese [8].

4. *Resistivity Model*

MACH3 incorporates a variety of physical models to compute the electric resistivity including scalar resistivity based on the Spitzer electron–ion collision frequency, constant resistivity, neutral resistivity based on both electron–ion and electron–neutral collisions, and a tabular form obtained from the SESAME data library.

The computations presented here use both Spitzer resistivity, constant resistivity, and a new Braginskii resistivity model that accounts for the tensor nature of electric resistivity[‡]. Specifically, in the presence of a magnetic field, the resistivity perpendicular to the magnetic field

$$\eta_{\text{perp}} \approx 2.0 \cdot \eta_{\text{par}} \tag{4}$$

and the parallel component

[‡]Personal communication with I. G. Mikellides, June 2007.

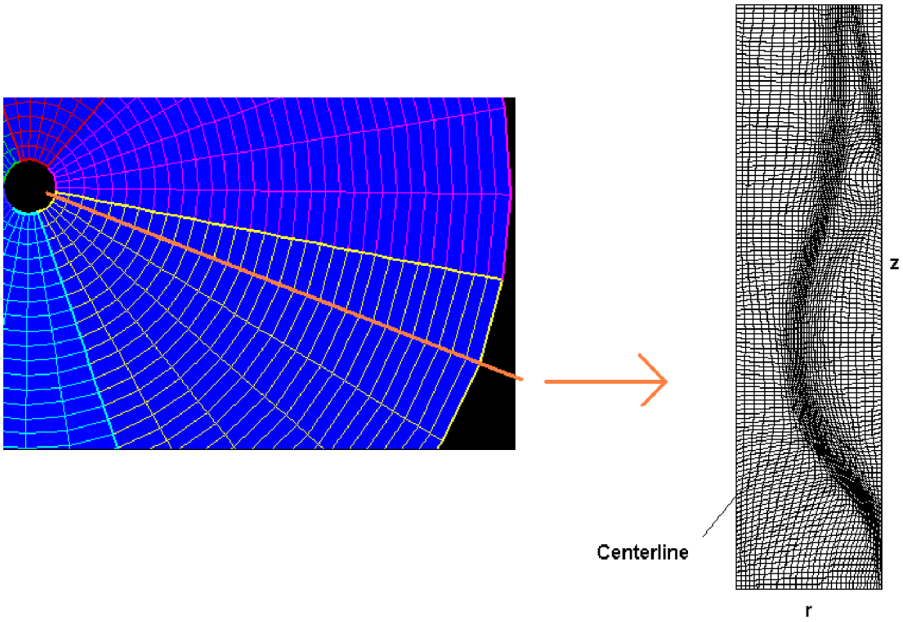

Fig. 4 A slice along a line of constant theta, showing the mesh which conforms to the physical gradients in the radial and axial directions.

$$\eta_{\text{par}} \approx \eta_0 \tag{5}$$

where η_0 is the Spitzer resistivity. MACH3 calculates these transport coefficients as

$$\eta_0 = 5.2 \cdot 10^{-5} \frac{Z\,\ell_n\,\Lambda}{T_e^{3/2}(\text{eV})} \tag{6}$$

$$\eta_{\text{par}} = g_e \eta_0 \alpha_0 \tag{7}$$

and

$$\eta_{\text{perp}} = g_e \eta_0 \left[1 - \frac{\alpha_1' x_e^2 + \alpha_0'}{x_e^4 + \delta_1 x_e^2 + \delta_0}\right] \tag{8}$$

where

$$x_e = \frac{qB}{m_e} T_e = \omega_B T_e \tag{9}$$

and g_e, α, and δ are polynomial fits to the Braginskii constants. For fully doubly ionized helium, these are $g_e(2) = 2.284$, $\alpha_0(2) = 0.441$, $\alpha_0'(2) = 0.595$, $\alpha_0''(2) = 0.344$, $\alpha_1'(2) = 5.523$, $\delta_0(2) = 1.05$.

The Generalized Ohm's Law is written as

$$\eta \bar{J} = \bar{E} + \bar{v} \times \bar{B} - \frac{1}{en_e}(\bar{J} \times \bar{B}) + \frac{1}{en_e}\bar{\nabla} p_e \tag{10}$$

MACH3 solves the magnetic induction equation by taking the curl of Eq. (10) and using Faraday's law to eliminate the electric field:

$$\bar{\nabla} \times \eta \bar{J} = \frac{-\partial \bar{B}}{\partial t} + \bar{\nabla} \times \bar{v} \times \bar{B} - \bar{\nabla} \times \frac{1}{en_e}(\bar{J} \times \bar{B}) + \bar{\nabla} \times \frac{1}{en_e}\bar{\nabla} p_e \tag{11}$$

where the last two terms on the right-hand side represent the Hall effect and contributions from the electron thermal pressure gradient. Considering an ideal gas, $p_e = n_e k T_e$ the last term becomes $(en_e)^{-1}\bar{\nabla} n_e \times k\bar{\nabla} T_e$, which can be generally neglected in such magnetic confinement schemes since predominantly the density gradient is parallel to the temperature gradient. The magnitude and significance of the Hall current scale with the Hall parameter, which can be written in terms of characteristic plasma/field properties as $\Omega = B/\eta e n_e$ where the characteristic magnetic field, $B \sim 1T$, the characteristic electrical resistivity, $\eta \sim 2 \times 10^{-6}$ Ωm and the electron number density for fully doubly ionized He, $n_e \sim 1.22 \times 10^{22}/\text{m}^3$. This results in hall parameters of the order of 250 for the magnetic rocket scheme which in turn indicate that the significant hall currents generated will interact with the magnetic field to cause substantial plasma rotation. The highly 3-D flow emerging from such interactions does not lend itself to closed-form analytic solutions and hence inclusion of the Hall effect does not permit code verification. The main objective of this study is to produce 3-D numerical simulations of magnetic nozzle flow that can be verified by comparisons to analytic solutions, thus the Hall effect is excluded. This does not detract from the actual application value of the simulations as experiments can be designed such that the hall current is shorted out. This can be accomplished by application of a thin insulating material along the solenoidal magnet's interior surface [9]. Such experiments can then be used to provide further validation of the code's results and isolate the effects of finite resistivity. Hence, the form of Ohm's law used in this numerical study, represented by the magnetic induction equation (after invoking Ampere's law) $\frac{\partial \bar{B}}{\partial t} = \bar{\nabla} \times \bar{v} \times \bar{B} - \bar{\nabla} \times \eta \bar{J}$ also allows independent study of the effects of finite electrical resistivity on the integrity of the magnetic confinement, acceleration, and overall magnetic rocket performance.

MACH3 incorporates the Braginskii resistivity by calculating the left hand side of Eq. (10) in component form:

$$\begin{aligned} \eta J_x &= \eta_{\text{perp}} J_x + (\eta_{\text{par}} - \eta_{\text{perp}}) J_{\text{par},x} \\ \eta J_y &= \eta_{\text{perp}} J_y + (\eta_{\text{par}} - \eta_{\text{perp}}) J_{\text{par},y} \\ \eta J_z &= \eta_{\text{perp}} J_z + (\eta_{\text{par}} - \eta_{\text{perp}}) J_{\text{par},z} \end{aligned} \tag{12}$$

The parallel and perpendicular components of the current J are computed as projections onto the magnetic field lines, with the components of the resistivity given by Eqs. (7) and (8).

5. *Grid Sensitivity*

The simulations presented in this paper used a $32 \times 36 \times 130$ (radial $\times$ azimuthal $\times$ axial) grid resolution. The primary constraint in the selection of the grid is accurate resolution of the plasma-field interface. The extent of numerical diffusion on the simulations was shown to be minimal after simulations with a finer grid were performed. Previous simulations in two dimensions (radial and axial) showed no major differences between cases of different mesh configurations provided there are enough nodes to resolve the steep

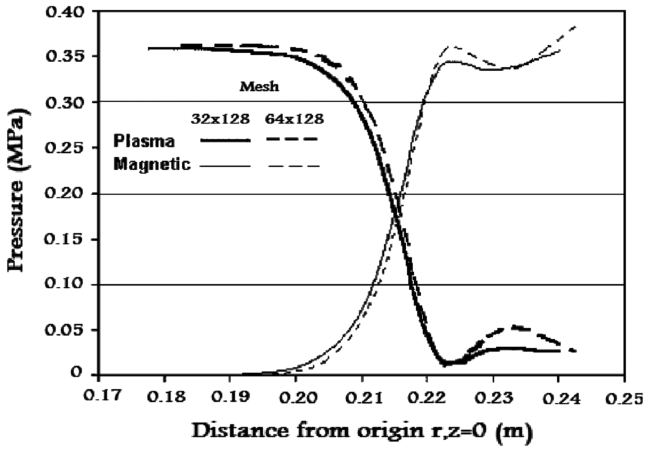

Fig. 5 Comparison of plasma and magnetic pressures near the stagnation region using a two-dimensional simulation with 32 × 128 and 64 × 128 cells [3].

gradients in the region. Specifically, 2-D simulations involving 32 × 128 cells (radial × axial) showed no appreciable difference when compared with simulations involving 64 × 128 cells (Fig. 5). A comparison of plasma and magnetic pressure profiles across the current layer, near the stagnation region, revealed little difference between the two cases. Simulations in three dimensions conducted with 36 azimuthal cells limited the magnitude of the oscillations as the solution approached steady state without needlessly limiting the size of the cells near the centerline, and thus maintained reasonable computational times. Additional simulations conducted with 54 azimuthal cells showed negligible differences from 36 azimuthal cells when comparing the pressure profiles across the current layer.

III. Results and Analysis

The various convective and diffusive processes present within the plasma-field interaction region lead to deviations of the magnetic nozzle flow from that of a solid-wall C-D nozzle. In an ideal MHD simulation, the thermal pressure would be exactly balanced by the Lorentz Force generated within an infinitely thin current layer. In a numerical MHD simulation modeled with finite resistivity, the current layer exists as a gradient, leading to more interaction between the plasma and magnetic field which results in a reduction of axial thrust. Other effects can lead to deviations from isentropic flow as well, such as mass-flux penetration into the current layer and the presence of the magnetic field in the plasma flow region. The numerical models are analyzed and compared with an equivalent isentropic nozzle to determine the magnetic nozzle performance.

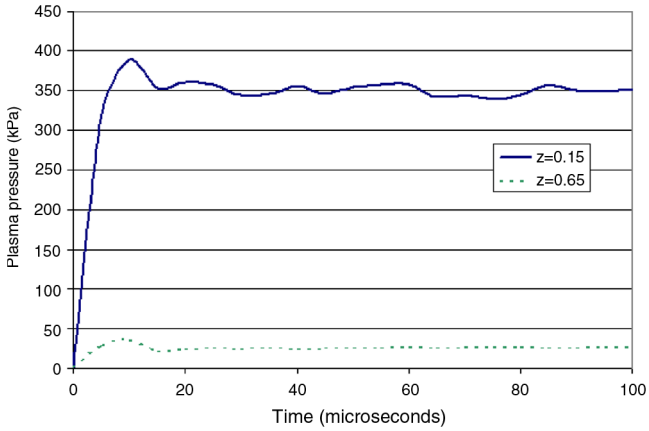

Fig. 6 Pressure profiles at various locations showing the time evolution of the flow.

A. Depiction of the Nozzle Flow

Numerical modeling of steady-state magnetic nozzle flows required monitoring the evolution of flowfield parameters to evaluate the necessary characteristic times to reach steady state. A typical evolution is depicted by Fig. 6. After an initial transient period, the flow reached a steady-state near 20 microseconds and was allowed to run until 100 microseconds to ensure that any oscillations were dampened as much as possible.

Figures 7 and 8 show the steady-state distributions of plasma density and magnetic field, respectively, in a sample simulation. The flow exhibits the classic bell shape associated with the converging–diverging nozzle expansion. The density decreases as it approaches the throat, and then continues to decrease as it expands downstream to supersonic velocities. Figure 9 shows the density, Mach number, and magnetic pressure r-z distributions at various locations along the nozzle. There exists a region of roughly uniform flow extending from the center axis of the nozzle to near the current layer.

The r-θ distributions confirm the expected axisymmetry. The small fluctuations in both the density and magnetic field are negligible. Most of the small variations exist near the sharp gradients of the plasma-field interaction and do not contribute to the overall results. Also, near the centerline, there is difficulty in resolving the flow due to the clustering of a large number of irregularly shaped grid cells.

The magnetic pressure has not been completely excluded from the region of plasma flow, as was seen in previous two-dimensional simulations. The thermal pressure at the throat is approximately 0.170 MPa, which is not sufficient to balance the magnetic pressure which, before compression, is approximately 0.355 MPa. The remaining magnetic pressure in the region of plasma flow will act as a drag force, causing deviations from isentropic calculations that will be examined.

Finally, the two expected regions of uniform plasma flow and plasma free magnetic field are separated by a region of plasma-field interaction (Fig. 10). In this region, the various convective and diffusive processes between the plasma and magnetic field cause considerable deviation from isentropic flow, and will be dependent on the choice of resistivity model used for the computations.

B. Resistivity Effects and Mass Loading

The flow parameters of the nozzle are expected to be heavily dependant on the choice of the resistivity model in MACH3. For example, the resistivity perpendicular to the magnetic field using tensor resistivity is approximately twice that for a classical Spitzer model, leading to a potentially thicker current layer, and thus greater deviation from isentropic flow. While the exact characteristics of isentropic flow have yet to be identified, it is clear that increased plasma-field interaction within the current layer will lead to a reduction of measurable axial thrust at the exit as it results in a loss of kinetic energy within the flow, and this can be compared between models. In addition to this, the effects of resistivity can be further investigated by implementing the constant resistivity model.

1. Dependency of Current Layer Thickness on Electrical Diffusivity

A quantitative analysis of the current layer thickness as a function of the resistivity is possible by using the magnetic diffusion equation

$$\frac{\partial \bar{B}}{\partial t} = -\bar{\nabla} \times \left(\frac{\eta}{\mu_0} \bar{\nabla} \times \bar{B} \right) \tag{13}$$

This can be nondimensionalized to the more useful form

$$\frac{\partial \tilde{B}}{\partial \tilde{t}} = \frac{\alpha_0 \tau}{\delta^2} [-\tilde{\nabla} \times (\tilde{\alpha}\, \tilde{\nabla} \times \tilde{B})] \tag{14}$$

where τ is a characteristic time, α is the electric diffusivity, and δ is the thickness of the current layer. From Eq. (14), the current layer thickness can be approximated as

$$\delta \approx \sqrt{\alpha_0 \tau} \tag{15}$$

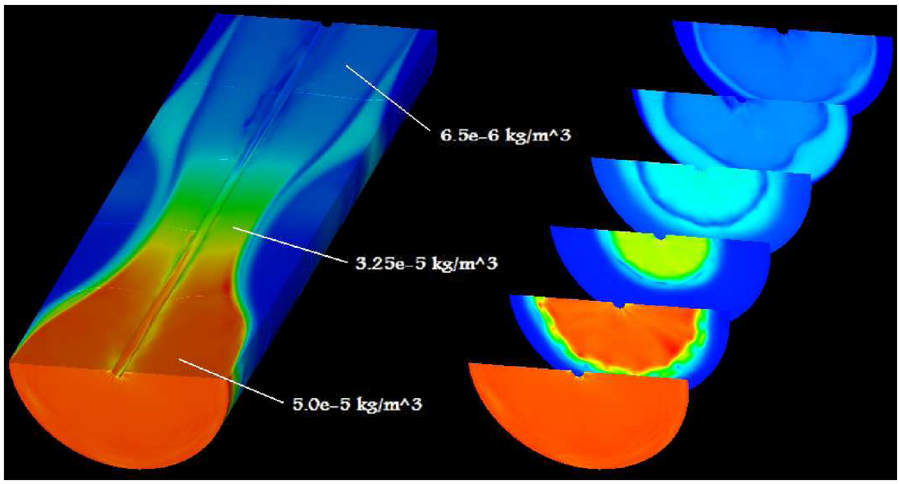

Fig. 7 Steady-state density distributions.

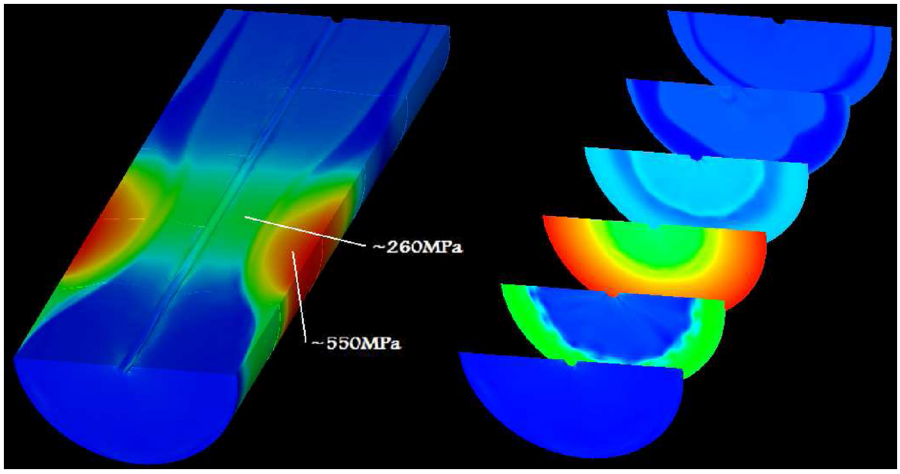

Fig. 8 Steady-state magnetic pressure distributions.

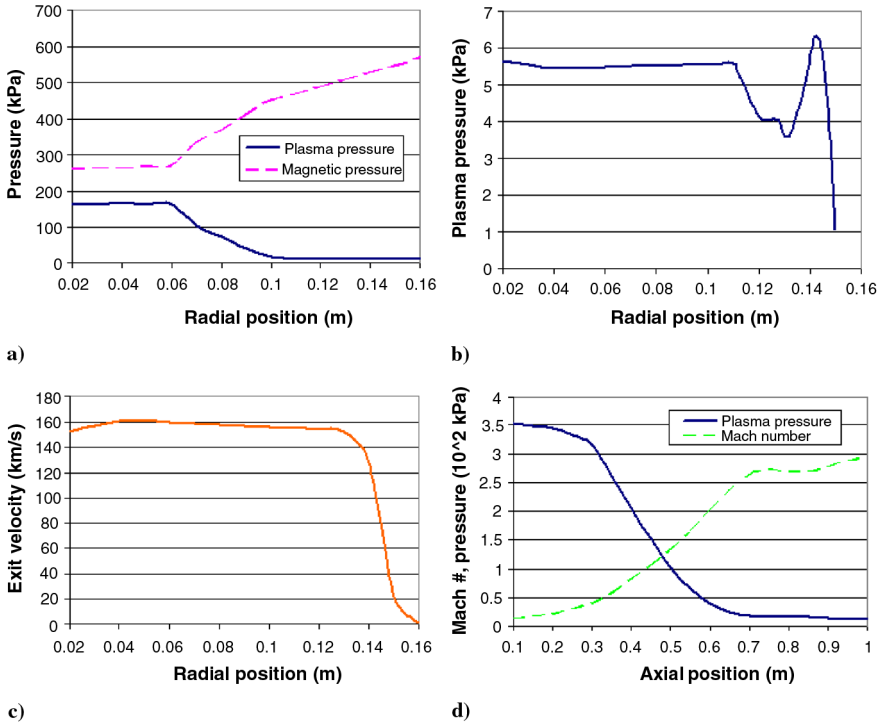

Fig. 9 Plots at various locations in the magnetic nozzle depicting a) plasma and magnetic pressure profiles near the throat, b) plasma pressure profile at the exit, c) velocity profile at the exit, and d) plasma pressure and Mach number profiles near the centerline.

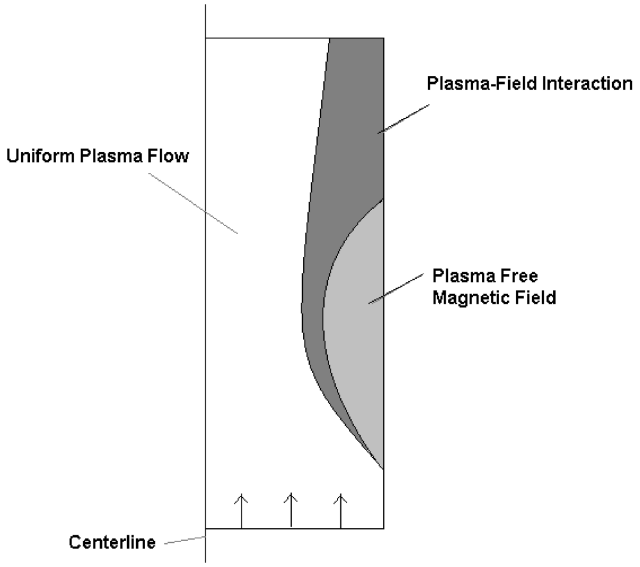

Fig. 10 Depiction of the three regions of plasma flow, magnetic field, and plasma-field interaction.

which is accurate to an order of magnitude and dictates that the thickness scales as the square root of the resistivity (or diffusivity). Thus, when comparing results from the Braginskii model with the classical model, it is expected that the current layer of the classical model will be roughly 70% as thick as that of Braginskii, and this in turn will lead to a simulation with smaller plasma-field interactions, and thus a higher mass-flow rate and thrust.

The differences in the current layer thickness and the deviation from isentropic flow between the resistivity models can be enhanced by the use of the constant resistivity model. From the classical Spitzer model with throat temperature $T_e = 75$ eV, Eq. (6) gives the diffusivity at the throat as roughly 1.25 m^2/s. For Braginskii this is about 2.50 m^2/s. For the constant model, the diffusivity was selected as 0.001 m^2/s, a drop of 3 orders of magnitude. It would be expected from Eq. (15) that the thickness would drop to approximately 3% that of the classical model. This should provide the closest simulation to that of an ideal MHD model, or a solid wall nozzle, and exhibit flow parameters that more closely resemble isentropic calculations.

Table 1 shows the effects of different resistivity models on the total mass-flow rate and thrust, and the exit Mach number and exhaust velocity computed in the region of uniform flow. The flow properties exhibit negligible change when compared with different resistivity models. This is in contrast with the expectations regarding a current layer dependence on the resistivity, which in turn will affect thrust performance. It would be expected that the classical simulations show a higher total mass-flow rate and thrust compared with Braginskii, and that the constant simulation, with very low resistivity, show a much higher mass-flow rate and thrust. Figure 11 shows the pressure profiles plotted at the throat as a function of radial location for the various resistivity models, indicating similar current layer thicknesses ($\delta \sim 3.5$ cm) contrary to the expectations from Eq. (15). Thus, the conclusion here is that magnetic diffusion is not the dominant effect controlling the thickness of the current layer.

2. *Dependency of Current Layer Thickness on Mass-Flux Penetration*

Equation (13) dictates that for static plasma the Lorentz force must balance the pressure gradient of the thermal plasma. For high-speed

Table 1 Comparisons between simulations conducted with three different resistivity models

Model	M-F-R, g/s	Thrust, N	Mach number	Exhaust V, m/s
Braginskii	58.7	9044	2.89	159320
Classical	56.5	8773	2.99	160400
Constant	55.2	8650	2.80	157960

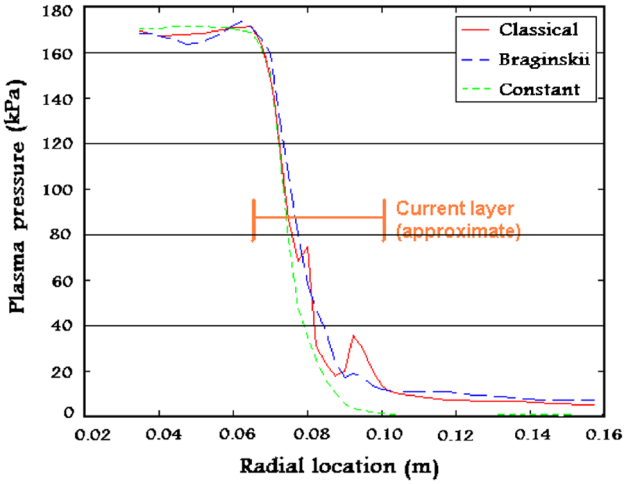

Fig. 11 Depiction of the plasma pressure near the throat as a function of radial location. The approximate thickness of the current layer does not appreciably change for different resistivity models ($\delta \sim 3.5$ cm).

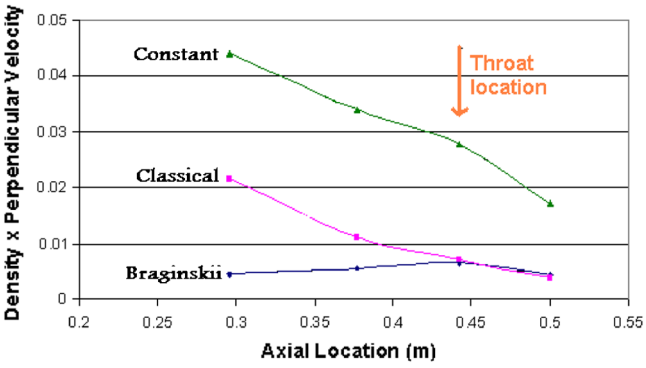

Fig. 12 Mass-flux penetration into the current layer, nondimensionalized with respect to the stagnation density and throat velocity.

plasma flow, there exists the possibility that a fraction of the incident plasma penetrates the current layer at some finite perpendicular velocity. For this scenario, the Lorentz force must balance the momentum of the mass-flux penetration in addition to the thermal pressure. The hydrodynamic balance is then

$$\rho\bar{u}\cdot\nabla\bar{u} + \nabla p = \bar{j}\times\bar{B} \tag{16}$$

This indicates that convection should also be considered in the evaluation of the current layer thickness, changing Eq. (13) to

$$\frac{\partial\bar{B}}{\partial t} = \bar{\nabla}\times(\bar{u}\times\bar{B}) - \bar{\nabla}\times\left(\frac{\eta}{\mu_0}\bar{\nabla}\times\bar{B}\right) \tag{17}$$

Nondimensionalizing Eq. (17) gives

$$\frac{\partial\tilde{B}}{\partial\tilde{t}} = \frac{u_{\text{perp}}\tau}{\delta_C}[\tilde{\nabla}\times(\tilde{u}\times\tilde{B})] + \frac{\alpha_0\tau}{\delta_D^2}[-\tilde{\nabla}\times(\tilde{\alpha}\,\tilde{\nabla}\times\tilde{B})] \tag{18}$$

where u_{perp} is the component of velocity perpendicular to the magnetic field lines and δ_C and δ_D are the characteristic thicknesses of the current layer as determined by convection and diffusion, respectively. From Eq. (18), these are $\delta_C \sim \tau u_{\text{perp}}$ and $\delta_D \sim (\tau\alpha)^{1/2}$, which again are accurate to within an order of magnitude and allow for comparison between convective and diffusive processes within the layer. Figure 12 depicts the mass flux into the current layer as a function of axial location as computed by

$$\rho u_{\text{perp}} = \rho\sqrt{|V|^2 - \bar{V}\cdot\left(\frac{\bar{B}}{|B|}\right)} \tag{19}$$

Table 2 Values of δ_C/δ_D for the three simulations as evaluated at two locations. The ratio δ_C/δ_D dictates the dependence of the current layer thickness on convective processes over diffusive processes

Location	Braginskii	Classical	Constant
Upstream ($z = 0.30$ m)	0.445	3.91	233
Throat ($z = 0.44$ m)	0.785	1.22	208

Figure 12 dictates a higher mass flux for the classical and constant resistivity simulations than for Braginskii, indicating higher dependence on convective processes in determination of current layer thickness. Because Braginskii has a higher resistivity than the classical simulation, and a much higher resistivity than the constant simulation, it is expected that the Braginskii simulation will show less dependence on mass-flux penetration in the determination of the current layer thickness. Tabulated values for the ratio δ_C/δ_D dictate the dependence of the current layer thickness on the ratio of convective processes to diffusive processes (Table 2). The characteristic time is selected as the throat radius divided by the throat velocity, giving $\tau = 1$ μs. For $\delta_C/\delta_D \gg 1$ convection will dominate, where as for $\delta_C/\delta_D \ll 1$ diffusion will dominate.

For the Braginskii simulation, the ratio δ_C/δ_D indicates more dependence on diffusion than convection. The Classical simulation favors convection upstream with roughly equal dependence near the throat. For the constant simulation, with the diffusivity set to 3 orders of magnitude less, the convective terms clearly dominate the determination of the current layer thickness.

Additionally, the magnetic Reynolds number

$$R_m = \frac{uL}{\alpha} \tag{20}$$

which is the ratio of the convection of the magnetic field to the diffusion of the magnetic field, can be used in the same fashion. Using $u = u_{\text{perp}}$ and $L = \delta$ at the upstream location gives $R_m = 8.8$, 110, and 2.6×10^5 for the Braginskii, Classical, and Constant simulations, respectively. These values for the magnetic Reynolds number confirm that the thickness of the current layer shows increased dependence on convection as the diffusivity of the model is decreased.

While the selection of resistivity model showed negligible differences for the mass-flow rate, total thrust, and approximate current layer thickness, it is clear that the physics involved in the formation of the layer is highly dependent on the model. Depending on the magnitude of the resistivity, the current layer that would be produced from purely diffusive effects may be not be sufficient to balance out the dynamic pressure of the plasma. If this is the case, the momentum of the plasma will result in mass penetration into the current layer. This convective effect will then increase the thickness of the current layer, reestablishing equilibrium. The combined diffusive and convective effects essentially define a minimum thickness for the current layer (about 3.5 cm at the throat) that is required to maintain equilibrium.

C. Flow Characterization

Two simulations were conducted with classical Spitzer resistivity to capture the expected dependence of the exhaust velocity on the square root of the stagnation temperature. The simulations were performed with fixed stagnation pressure ($P_0 = 0.355$ MPa) and applied field, but varying the stagnation temperature, 100 eV $\leq T_0 \leq$ 200 eV. Figure 13 depicts this dependence. The numerical results (in the region of uniform flow) are compared with the idealized isentropic expression for the exhaust velocity

$$U_e = \sqrt{\frac{2\gamma(1+Z)RT_0}{\gamma-1}\left[1-\left(1+\frac{\gamma-1}{2}M^2\right)^{-1}\right]} \tag{21}$$

with Mach number $M = 2.75$, as computed by both simulations in the region of uniform flow. The computed exhaust velocity from MACH3 shows excellent agreement with Eq. (21) indicating that the magnetic nozzle operates as an equivalent solid wall nozzle of area ratio $A_e/A_* = 2.54$ and design Mach number 2.75. It should be noted here that due to time constraints, this data was obtained from a computational region with lower grid density and used the classical resistivity model. The design Mach number is slightly lower than that of the higher grid density Braginskii simulations presented in the next section, however, the conclusion remains the same; the exhaust velocity appropriately scales as the square root of the stagnation temperature, and thus comparisons can be made with a solid wall nozzle of equivalent design Mach number.

Table 3 Comparisons with values taken from MACH3 computations and isentropic calculations based on the computed Mach number

Location	Model	ρ_0/ρ	T_0/T	P_0/P
Throat	Isentropic flow	1.54	1.33	2.05
——	MACH3 (Braginskii resistivity)	1.58	1.37	2.13
Exit	Isentropic flow	6.98	3.65	25.47
——	MACH3 (Braginskii resistivity)	7.69	3.60	27.62

D. Magnetic Nozzle Performance and Isentropic Flow Comparisons

The isentropic equations for a converging–diverging nozzle can be used to compare the magnetic nozzle with a solid-wall nozzle. Also of use is the isentropic calculation of the area ratio

$$\frac{A_*}{A} = \left(\frac{\gamma+1}{2}\right)^{\frac{\gamma+1}{2(\gamma-1)}} M\left(1+\frac{\gamma-1}{2}M^2\right)^{-\frac{\gamma+1}{2(\gamma-1)}} \tag{22}$$

Once the throat area is known, the isentropic mass-flow rate can be calculated as

$$\dot{m} = \sqrt{\gamma\rho_0 P_0}\left(\frac{2}{\gamma+1}\right)^{\frac{\gamma+1}{2(\gamma-1)}} \qquad A_* = \frac{9}{16}\sqrt{\gamma\rho_0 P_0}A_* \tag{23}$$

with the thrust given by

$$T = \dot{m}U_e \tag{24}$$

This thrust and mass-flow rate can be compared with values from MACH3 computed at the exit.

Flow parameters in this region of uniform flow are presented in Table 3 along with equivalent isentropic calculations. The isentropic values were calculated with $M = 1$ for the throat and $M = 2.82$ for the exit, as computed from MACH3. The computed values and isentropic calculations show reasonable agreement for the flow parameters near the throat. At the exit, the computed values for the pressure and density are roughly 10 and 8% lower than isentropic values, respectively, however, the exit temperature shows better

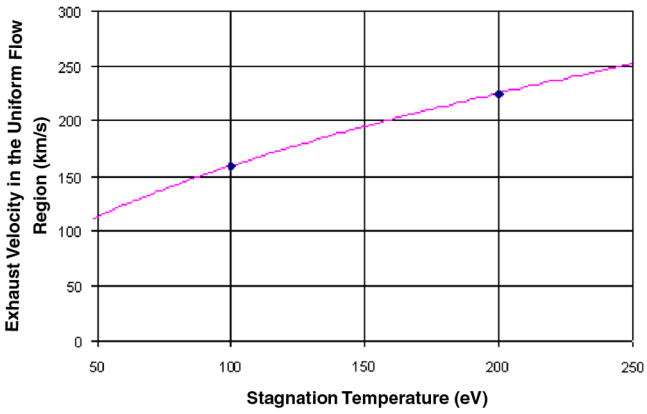

Fig. 13 Exhaust velocity in the region of uniform flow as a function of the stagnation temperature. The curve represents Eq. (21) with a Mach number of 2.75, showing excellent agreement with computed results.

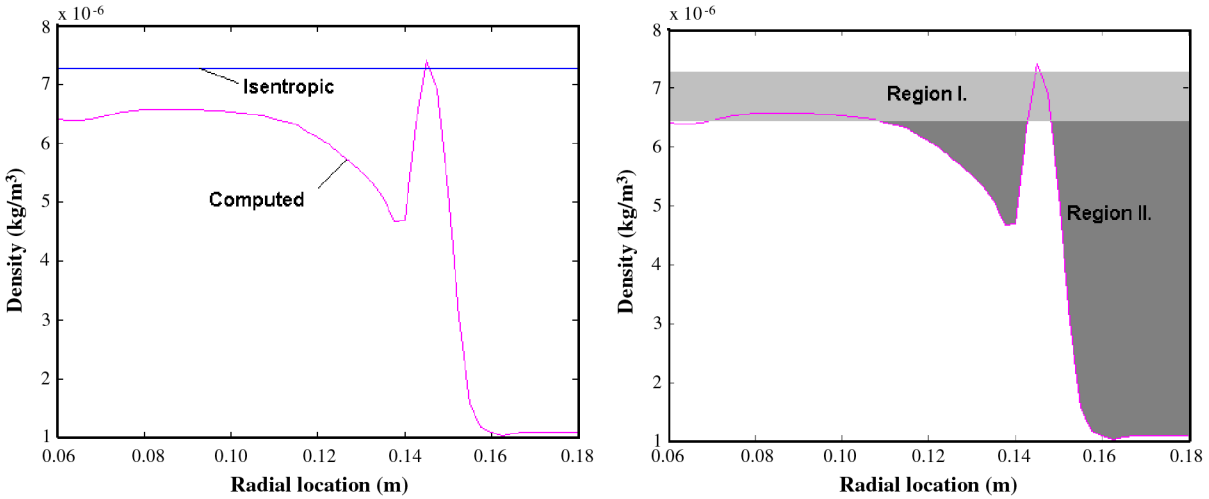

Fig. 14 Density profile at the exit along a slice of constant theta, depicting flow reductions due to the presence of magnetic pressure in the region of uniform flow (region I) and the plasma-field interaction within the current layer (region II).

agreement. We speculate that this is indicative of the magnetic pressure still present in the plasma flow region acting as a drag force on the plasma as it transits the nozzle. This drag force will serve to decrease the plasma pressure and density in the region of uniform flow, leading to a reduction in mass-flow rate and thrust. This is in addition to the reduction that is a result of the plasma-field interaction. These reductions can be quantified with a comparison to an isentropic solid-wall nozzle of equivalent Mach number design ($M = 2.82$).

From Eq. (22), $M = 2.82$, and a known exhaust exit area of 1018 cm^2, the area of the throat for isentropic calculations is $A_* = 382.9$ cm^2 or $R_* = 11.0$ cm. From Eq. (23), the isentropic mass-flow rate is calculated as $\dot{m} = 122$ g/s. Using this along with Eqs. (21) and (24) gives the isentropic exhaust velocity and the thrust: $U_e = 160.55$ km/s and $T = 19.5$ kN.

Integration over the MACH3 exit profiles provides the computed values for the mass-flow rate and the total thrust. Specifically, values for the quantities were obtained by summation over all radial and aximuthal cells at the exit as follows:

$$\dot{m} = \sum_i \rho_i U_i \Delta A_i \tag{25}$$

and

$$T = \sum_i \rho_i U_i^2 \Delta A_i \tag{26}$$

The computed values were obtained as $\dot{m} = 62.7$ g/s and $T = 9616$ N. Thus, the simulation of the nonideal MHD nozzle produces approximately 49.2% as much thrust as a solid wall nozzle of equivalent Mach number design. Further analysis leads to the sources of the reductions, which can be considered the result of two effects: the drag effect of the magnetic field within the region of uniform plasma flow and the plasma-field interaction within the current layer.

In the region of uniform flow, the computed and isentropic exhaust velocity differ by less than 1%. Thus, looking at Eqs. (25) and (26), the reduction of axial thrust in this region must be a result of the computed plasma density being lower than that of the calculated isentropic plasma density. It should be mentioned here that there exist small numerical fluctuations in the value of the flow parameters in the region of uniform flow. The values depicted in Table 1 were an average of the computed values that exist within the region of uniform flow.

Figure 14 compares the radial profile of the plasma density at the exit plane along a line of constant theta to the isentropic value. On the right, region I depicts the area of the mass-flow rate reduction due to the presence of magnetic pressure in the flow region. This is a result of having lower exit density in the uniform flow than that calculated isentropically. The difference between computed and isentropic density results in the reduction of approximately 2260 N of thrust, or approximately one quarter of the total thrust loss. The remainder of the thrust reduction, 7620 N, is a result of the physical processes within the current layer, depicted in Fig. 14 in region II.

The efficiency of the thrust can be computed using

$$\eta_{\text{eff}} = \frac{1/2\dot{m}U_{\text{ex}}^2}{\dot{m}h_0} = \frac{T^2}{2\dot{m}^2 h_0} \tag{27}$$

where h_0 is the stagnation enthalpy, equivalent to the specific heat at constant pressure multiplied by the stagnation temperature. Equation (27) gives an efficiency of 11.0%.

IV. Conclusions

The computational tool MACH3 was successfully implemented to analyze the physical processes within a three-dimensional magnetic nozzle flow. The work provided necessary upgrades to the MACH3 code and verified the magnetic nozzle model by comparisons to isentropic nozzle flows of equivalent exit Mach number design.

The MACH3 computational code was appropriately suited to model magnetic nozzle flow due in part to its arbitrary coordinate system, nonideal computation of resistive effects, grid adaptation schemes, and treatment of vector components and gradients in all three dimensions. The code was sufficiently upgraded to compute an initial solenoidal magnetic field, import an external mesh from GridGen3D, dynamically adapt to physical functions, and account for the tensor nature of resistivity with Braginskii coefficients. Most of these upgrades were completed in such a fashion as to allow for their use in future problems unrelated to the current work, and thus contribute to the overall growth of the code.

Analysis of the plasma-field interaction indicated that if diffusive processes are insufficient to generate a large enough current layer such that the Lorentz force will balance the dynamic pressure, then the momentum of the plasma will result in a mass-flux penetration of the layer, increasing the thickness and reestablishing equilibrium. This essentially defines a minimum thickness of the current layer, which is approximately 3.5 cm at the throat.

A simulation with higher stagnation temperature, but fixed stagnation pressure and applied field, produced the expected dependence of the exhaust velocity in the region of uniform flow on the square root of the stagnation temperature, which demonstrates that the magnetic nozzle scales appropriately as a solid wall nozzle of equivalent Mach number design.

The various physical processes within the nozzle led to a reduction of approximately 50% of the mass-flow rate and thrust when compared with an isentropic nozzle. These effects are shown to be independent of grid selection. Approximately 1/4th of this reduction is due to the presence of magnetic pressure within the region of uniform plasma flow acting as a drag force, with the remainder a result of plasma-field interaction within the current layer.

Acknowledgments

The authors would also like to thank Kyle Squires, Don Boyer, Carl Covatto, Dan Stanzione, Karl Lindekugel, and Brian Parma for providing their insights into this work. The authors also benefited from conversations with Ioannis Yiangos Mikellides of Jet Propulsion Laboratory, California Institute of Technology and Uri Shumlak of the University of Washington.

References

[1] Williams, C. H., and Borowski, S. K., "An Assessment of Fusion Space Propulsion Concepts and Desired Operating Parameters for Fast Solar System Travel," AIAA Paper 97-3074, July 1997.

[2] Peterkin, Robert E., Jr., and Frese, Michael H., *MACH: A Reference Manual*, 1st ed., Air Force Research Laboratory: Phillips Research Site, Albuquerque, NM, 1998.

[3] Mikellides, Pavlos, G., "An Overview of the MHD Code, MACH," AIAA Paper 2007-5614, July 2007.

[4] Mikellides, Ioannis, G., Mikellides, Pavlos, G., Turchi, Peter, J., and York, Thomas, M., "Design of a Fusion Propulsion System-Part 2: Numerical Simulation of Magnetic-Nozzle Flows," AIAA Paper 2000-3367, July 2000.

[5] Mikellides, Pavlos, G., "A Theoretical Investigation of Magneto-plasmadynamic Thrusters," Ph.D. Dissertation, Department of Aeronautical and Astronautical Engineering, Ohio State Univ., Columbus, OH, 1994.

[6] Gridgen Tutorial Workbook, Pointwise, 2006.

[7] Brackbill, J. U., "Coordinate System Control: Adaptive Meshes," *Numerical Grid Generation*, edited by J. F. Thompson, Elsevier Science, New York, 1982.

[8] Frese, M. H., "A Two-Dimensional Complex Region Mesh Generator," Mission Research Corp. AMRC-R-687, Albuquerque, NM, Feb. 1985.

[9] Gerwin, R. A., "Integrity of the Plasma Magnetic Nozzle," NASA Technical Rept. 2009-213439, Dec. 2009.

D. Gaitonde
Associate Editor